THE JOURNAL OF PHYSICAL CHEMISTRY C

Article

pubs.acs.org/JPCC

# Toward Understanding the Photocatalytic Activity of $PbMoO_4$ Powders with Predominant (111), (100), (011), and (110) Facets. A Combined Experimental and Theoretical Study

M. R. D. Bomio,*[,†] R. L. Tranquilin,[‡] F. V. Motta,[†] C. A. Paskocimas,[†] R. M. Nascimento,[†] L. Gracia,[‡,§] J. Andres,[§] and E. Longo[‡]

[†]LSQM- Laboratório de Síntese Química de Materiais - DEMat, Universidade Federal do Rio Grande do Norte - UFRN, P.O. Box 1524, Natal, RN 59078-97, Brazil

[‡]LIEC, Universidade Federal de São Carlos - UFSCar, P.O. Box 676, São Carlos, SP 13565-905, Brazil

[§]Departamento de Química Física y Analítica, Universitat Jaume I, 12071 Castello, Spain

Supporting Information

**ABSTRACT:** A complementary combination of experimental work and first-principle calculations, based on the density functional theory (DFT) method, has been used to increase our limited understanding of the enhanced photocatalytic activity of $PbMoO_4$ powders with predominant (111), (100), (011), and (110) facets. In this work, $PbMoO_4$ powders were prepared by the coprecipitation method and processed on a hydrothermal reactor at 100 °C/10 min. The variation of different types of modifiers such as acetylacetone (acac) or polyvinylpyrrolidone (PVP) is found to play a crucial role in controlling the particle size and morphology of products and their photocatalytic properties. The structure and morphology of these crystals were characterized by X-ray diffraction (XRD), micro-Raman (MR) spectroscopy, field-emission gun scanning electron microscopy (FEG-SEM), and ultraviolet visible (UV−vis) absorption spectroscopy. Furthermore, the as-synthesized $PbMoO_4$ micro-octahedrons without the presence of the (001) surface exhibit enhanced activity for the photodegradation of rhodamine B (RhB) under ultraviolet−visible light irradiation. On the basis of the theoretical and experimental results, we provide a complete assignment of the micro-Raman spectra of $PbMoO_4$, while a growth mechanism for the formation of $PbMoO_4$ micro-octahedrons was systematically discussed. A schematic illustration of the probable formation of morphologies in the whole of the synthetic process was also proposed, which reveals that the high photocatalytic activity is attributed to the absence of the (001) facet.

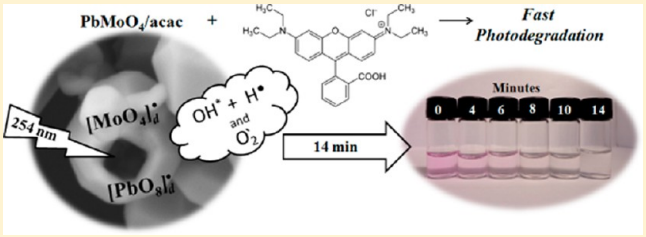


## 1. INTRODUCTION

Molybdates and tungstate-based oxides constitute an important class of materials that exhibit various functional properties; in particular, metal molybdates have received special attention due to their novel and intriguing properties for widespread technological applications.[1−11] Molybdates of relatively large bivalent cations (ionic radius >0.99 Å: Ca, Ba, Pb, Sr) usually exist in the so-called scheelite structure form[12] and have attracted considerable interest due to their promising technological importance in a broad range of applications such as photoluminescence, scintillator materials, humidity sensors, and catalysis.[13] As an important member of this family, lead molybdate ($PbMoO_4$) has gained increasing interest due to its use in a wide range of technological and theoretical fields,[12,14−24] and experimental studies on the optical properties of lead molybdate have been published by different research groups.[16,19,25−34]

$PbMoO_4$ crystallizes in a tetragonal scheelite structure having point group symmetry $4/m$ and space group $I41/a$, with two formula units per primitive cell,[5,6] and a specific feature of these systems is the existence of two different clusters in a crystal lattice, in which each Mo is surrounded by four equivalent O atoms composing the $[MoO_4]^{2-}$ tetrahedral configuration and each divalent metal, Pb, shares corners with eight adjacent O atoms, forming a $[PbO_8]^{2-}$ configuration.

The research in materials science to develop new properties and applications has been centered on the *bottom-up* approach. This technique is based on the construction of multifunctional nanostructures and devices by self-assembly of atoms and molecules.[35] The synthesis of micro- and nanoscale inorganic materials with special morphology, size, and hierarchy structure has attracted considerable attention in the past few decades due to their importance in basic scientific research and potential technological applications.[36,37] Recently, the synthesis of metal molybdates has attracted attention due to their potential application in several fields.[38−40] In particular, wet chemical synthesis (*bottom-up methods*) attracts great attention in the synthesis of $PbMoO_4$ crystals. The literature describes a range

**Received:** July 25, 2013
**Revised:** September 2, 2013
**Published:** September 12, 2013

of approaches for synthesizing several molybdates, in particular lead molybdates, by different procedures, such as solid state reaction,[41,42] Czochralski crystal growth,[43] chemical route,[44] galvanic cell method,[45] citrate complex,[46] sonochemical route,[47,48] microemulsion method,[49] microwave-assisted synthesis method,[50] precipitation method,[51,52] solvothermal route,[12] and hydrothermal method.[34,53,54] In this wide range of methods, in particular, the conventional hydrothermal (CH) method stands out because it uses environmentally friendly solvent, has low processing temperatures, and has reduced cost.

$PbMoO_4$ presents excellent optical and chemical properties due to its electronic structure and relatively low band gap energy as compared to the above scheelite structures and may be a promising photocatalyst. Therefore, it is of great importance to study the photocatalytic properties of this material for potential applications. It is well-known that photocatalytic processes occur on the surface of catalysts, and thus, size, shape, and exposed crystal facets of crystals play a critical role in the activity and efficiency of photocatalysts. The exposed facet of the $PbMoO_4$ crystal is an important factor influencing its photocatalytic performance. The essence of exposed facets is the surface atomic configuration and coordination, which show great effect on adsorption and reactivity of semiconductor materials. In this context, Shen et al.[54] and Hashin[55] have proved that $PbMoO_4$ microcrystals with a preferentially exposed (001) facet exhibit higher catalytic activity compared to that of the (100) facet, enhancing the photocatalytic activity for degradation of Rhodamine B (RhB) under light irradiation. Xing et al.[56] have obtained well-defined and uniform $PbMoO_4$ polyhedral crystals via a microemulsion-based solvothermal method, and the results of RhB photocatalytic degradation showed that these $PbMoO_4$ polyhedrons display excellent photocatalytic activity under visible ultraviolet light irradiation. Recently, Martínez de la Cruz et al.[57,58] successfully synthesized $PbMoO_4$ by a hydrothermal method in the absence of additives, and its photocatalytic activity was tested under UV irradiation for the degradation reaction of different organic dyes.

The aim of this work was to contribute to fill the gap between the single-crystal, powder, and microcrystalline worlds by comparing the surface properties of different facets of $PbMoO_4$, considered as models for mimicking the single-crystal world. Therefore, the validation of the photocatalytic activity of $PbMoO_4$ and the effect of the different facets are the focus of this contribution, in which new results on the synthesis of $PbMoO_4$ micro-octahedrons without the presence of (001) facets were examined. We have now discovered, by investigating a set of $PbMoO_4$ crystal facets with predominant (100), (110), (101), and (111) surfaces, that they present the highest photoreactivity. The materials were obtained by the coprecipitation method and processed by the hydrothermal method using two different modifiers at 100 °C for 10 min. These micro-octahedrons were analyzed by X-ray diffraction (XRD), micro-Raman (MR) spectroscopy, ultraviolet visible (UV−vis) absorption spectroscopy, and field-emission gun scanning electron microscopy (FEG-SEM), and a micro-octahedron growth mechanism is proposed and discussed in detail. The photocatalytic activity of the material was evaluated for the degradation reactions of rhodamine B (RhB). To complement these experimental measurements, the structural and electronic properties of bulk ground and triplet $PbMoO_4$ were investigated, as well as the catalytic activities of (001), (100), (110), (101), and (111) surfaces, using periodic density functional theory (DFT) computations and a slab model, and an explanation of the photocatalytic activity of $PbMoO_4$ powders without (001) facets is proposed. To our knowledge, this is the first report on the preparation of $PbMoO_4$ with unique structure and on its photocatalytic properties.

## 2. EXPERIMENTAL SECTION

**2.1. Synthesis of $PbMoO_4$ Crystals.** All chemicals used were analytical garde reagents without further purification, and $PbMoO_4$ (PMO) crystals were obtained by coprecipitation (CP) and hydrothermal methods in the presence of acetylacetone (acac) (Vetec) as a chelate modifier or polyvinylpyrrolidone (PVP) (Synth) as the coupling agent. The typical synthesis procedure is described as follows: 0.005 mol of molybdic acid ($H_2MoO_4$) (Synth) and 0.005 mol of lead nitrate [$Pb(NO_3)_2$] (Merck) and such amount of acac or PVP were dissolved in 75 mL of deionized water. Then, 5 mL of ammonium hydroxide ($NH_4OH$) (30% in $NH_3$, Synth) was added to the solution so that the pH value reached 11. These suspensions were stirred for 10 min by an ultrasound bath at room temperature. With this procedure, PMO crystals were obtained by the coprecipitation method. In a precipitation reaction, $Pb^{2+}$ cations are electron pair acceptors (Lewis acids), while $MoO_2^{4-}$ anions are electron pair donors (Lewis bases). The chemical reaction between these two species in solution results in the formation of PMO crystals as shown in the equations below

$$H_2MoO_{4(s)} + Pb(NO_3)_{2(s)} \xrightarrow{H_2O/acac/PVP} 2H^+_{(aq)} + 2NO^-_{3(aq)} + Pb^{2+}_{(aq)} + MoO^{2-}_{4(aq)} \quad (1)$$

$$Pb^{2+}_{(aq)} + MoO^{2-}_{4(aq)} \rightarrow PbMoO_{4(s)}\downarrow \quad (2)$$

These suspensions obtained were transferred into a stainless steel autoclave (lined with quartz glass), which was sealed and processed at 100 °C for 10 min using a heating rate fixed at 2 °C/min. After hydrothermal processing, the autoclave was cooled to room temperature. The resulting suspensions were washed several times with deionized water to neutralize the solution pH (≈7), and the white precipitates were dried with acetone and finally collected for characterization.

**2.2. Characterization of $PbMoO_4$ Crystals.** After hydrothermal processing at 100 °C for 10 min, PMO crystals were structurally characterized by XRD using a Rigaku-DMax/2500PC (Japan) with Cu−K$\alpha$ radiation ($\lambda$ = 1.5406 Å) in the $2\theta$ range from 10° to 75° with scanning rate of 0.02°/s and total exposure time of 15 min. In addition, the Rietveld routine was performed in the $2\theta$ range from 10° to 110°, using an angular step of 0.02°/s and total exposure time of 90 min. In this work, the profiles of the XRD experimental patterns observed for the $PbMoO_4$ crystals were refined with a theoretical line profile known as Crystallographic Information File (CIF) with ID code 1011170.[59] Micro Raman measurements were recorded using a T-64000 spectrometer (Jobin-Yvon, France) triple monochromator coupled to a CCD detector at 488 nm wavelength of an argon ion laser. Its maximum output power was kept at 10 mW with the use of a lens (100 $\mu$m) to prevent sample overheating. The morphologies were investigated using FEG-SEM (Carl Zeiss, model Supra 35-VP, Germany) operated at 6 kV. UV−vis spectra were taken using a Varian spectrophotometer, model


dx.doi.org/10.1021/jp407416h | J. Phys. Chem. C 2013, 117, 21382−21395

Cary 5G (USA), in diffuse reflection mode with MgO as standard.

**2.3. Photocatalytic Activity Measurement.** The photocatalytic properties of PMO crystals (as a catalyst agent) for the degradation of Rhodamine B (RhB) dye with molecular formula $[C_{28}H_{31}ClN_2O_3]$ (99.5% purity, Mallinckrodt) in an aqueous solution were tested under UV-light illumination. About 50 mg of catalyst crystals was placed in a 250 mL beaker, being added to 50 mL of RhB solution ($1 \times 10^{-5}$ mol $L^{-1}$) pH 4. These suspensions were ultrasonicated for 10 min in an ultrasonic cleaner before illumination and then stored in the dark for 5 min to allow the saturated absorption of RhB onto the catalyst. The beakers were then placed in a photoreactor at 20 $\mu$C and illuminated by six UV lamps (TUV Philips, 15 W, with maximum intensity at 254 nm). The power light was measured by Coherent Power Max model No PM10, and the optical energy density value was 20 mW $cm^{-2}$. At two-minute intervals, one 3 mL aliquot of these suspensions was removed and centrifuged at 9000 rpm for 5 min to remove crystals in suspension. Finally, variations of the maximum absorption band of supernatant solutions were monitored by UV−vis absorbance spectra measurements using a double-beam spectrophotometer with double monochromator and a JASCO photomultiplier tube detector (model V-660, USA).

## 3. COMPUTATIONAL SECTION

**3.1. Bulk.** Calculations for $PbMoO_4$ were performed using the CRYSTAL09[80] software package. The lead atom has been described by a Hay−Wadt pseudopotential scheme with large core, HAYWLC-2111dG, and molybdenum and oxygen centers by 976-6311d31G and 6-31d1G basis sets, respectively, which was taken from the Crystal Web site.[81] Becke's three-parameter hybrid nonlocal exchange functional[82] combined with a Lee−Yang−Parr gradient-corrected correlation functional (B3LYP)[83] was used. Diagonalization of the Fock matrix was performed at adequate *k*-point grids in the reciprocal space. The thresholds controlling the accuracy of the Coulomb calculation and exchange integrals were set to $10^{-8}$ (ITOL1 to ITOL4) and $10^{-14}$ (ITOL5), whereas the percentage of Fock/Kohn−Sham mixing matrices was set to 40.[80] Full optimization of scheelite-type $PbMoO_4$ cell parameters (*a* and *c*) and internal atomic position for the bulk $PbMoO_4$ were carried out.

**3.2. Surface Energy.** Surface energy is one of the key factors controlling the number of active sites and, accordingly, the photocatalytic activity of $PbMoO_4$. The low-index (001), (100), (110), (101), and (111) surfaces were modeled by unreconstructed (truncated bulk) slab models by using calculated equilibrium geometry. Because these surfaces have a different number of atoms in each layer to reach symmetry and stoichiometry, the low-index surfaces were modeled with different thicknesses in the *z*-direction but were periodic in the *x*- and *y*-directions. After the corresponding convergence test on the systems, slab models containing 15, 20, 15, 15, 12, and 50 atomic layers for the (001), (100), (110), (101), and (111) surfaces, respectively, were selected. For the models used here, bottom and top planes were equivalent in symmetry. A complete relaxation in each model was performed.

**3.3. Wulff Construction.** Gibbs defines[60] equilibrium morphology as the minimum energy conformation of faces of a fixed-volume crystal, which can be directly identified from the Wulff construction[61] on the polar plots of surface energies. It could be inferred that the faceted geometry of crystals is due to the existence of a finite number of minima in polar plots.[62] The theoretical equilibrium shape of a crystal is unique since, at a given temperature and pressure, it only depends on one thermodynamic property, i.e., on the ratio between specific surface energies (chkl) of different forms. Hence, predicting the equilibrium of a crystal can be reduced to calculating the chkl values without the presence of foreign adsorption (solvent and/or impurities), and the Wulff construction[61] is a standard method for determining the equilibrium shape of bulk crystals. The underlying basis for these size- and shape-dependent thermodynamic constructions states that the equilibrium shape of macroscopic crystals can be found by minimizing the surface energies with respect to a fixed volume as discussed in detail by Herring.[63] The energy of the terminated surface of a solid material is always higher than the bulk energy, and this energy difference is defined as the surface energy. On the basis of surface energies of all facets, the Wulff construction can be used to determine the equilibrium morphology of a material. Surface energy minimization is the central standard to optimize the composition of the crystal surface. The surface relative energy variations can basically be explained by the different chemical compositions of facets, which result in diverse degrees of broken chemical bonds on their surface[64−66] and sites. The shorter and stronger bonds in the surface skin (up to two or three atomic layers) dominate the size dependency, while bonds in the interior core remain in their bulk nature. Wulff construction[61,67] was applied to build theoretical crystals by using the ab initio calculated surface energies and the $PbMoO_4$ $I4_1/a$ crystal structure. The surface energy, $E_{surf}$, is defined as the total energy per repeating cell of the slab minus the total energy of the same number of atoms of the perfect crystal divided by the surface area per repeating cell of the two sides of the slab, i.e., $E_{surf} = (E_{slab} - nE_{bulk})/2A$. This equation has been used by us in previous studies.[31,68,69]

**3.4. Excited States.** Information on the excited states in tungstates and molybdates is deeply desired to understand the de-excitation processes after high-energy electronic excitation since these materials are widely used for scintillation detectors. Density functional theory (DFT) and its extensions have been used to understand the role of the electronic excited states in the PL behavior observed in scheelite-[33] and perovskite-based materials,[70] a fundamental issue that remains far from being fully understood. On the basis of the molecular orbital theory, Itoh and Kajitani[71] have recently reported that the intrinsic luminescence bands of $PbMoO_4$ originate from the radiative transitions from the triplet $^3T_1$ and/or $^3T_2$ states to the $^1A_1$ ground state and that the symmetry lowering of $(MoO_4)^{-2}$ ions from $T_d$ to $C_{3v}$ due to the Jahn−Teller effect could lift the degeneracy of the $^3T_1$ and $^3T_2$ states. The presence of excited electronic states and how they can be associated to in-gap defect states give rise to PL emissions. In addition, our investigations of different excited facets of $PbMoO_4$ may be helpful to comprehend the photoreactivity and catalytic activity of $PbMoO_4$.

To find the excited triplet electronic state, an initial dislocation from the ground state has been made to induce deformation on one $[MoO_4]$ cluster to a trigonal pyramid.[71] Then, a full optimization is performed. Vibrational analysis has been made to ensure that there are no imaginary frequencies and the structure corresponds to a minimum for the ground and excited triplet states. The band structures have been obtained along the appropriate high-symmetry paths of the Brillouin zone. Finally, the low-index (001), (100), (110), (101), and (111) surfaces were modeled at the triplet state

using the optimized geometry of the bulk in the excited triplet state.

## 4. RESULTS AND DISCUSSION

**4.1. X-ray Diffraction and Rietveld Analysis.** X-ray patterns of PMO/acac and PMO/PVP powders processed in the hydrothermal system at 100 °C for 10 min are presented in Figure 1. XRD patterns revealed that all diffraction peaks of

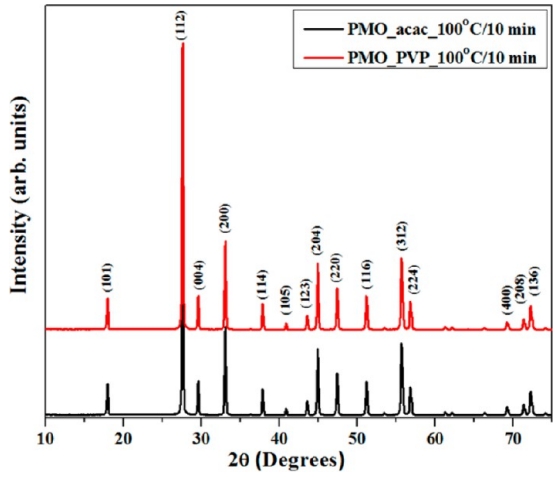


**Figure 1.** XRD patterns of $PbMoO_4$/acac and $PbMoO_4$/PVP micro-octahedrons processed by the hydrothermal method at 100 °C for 10 min.

PMO/acac and PMO/PVP micro-octahedrons can be indexed to the scheelite-type tetragonal structure without the presence of secondary phases, in agreement with the respective Joint Committee on Powder Diffraction Standards (JCPDS) card n°. 44-1486.[72] Moreover, the relative intensities and sharp diffraction of all peaks indicated that the materials are well-crystallized, suggesting an ordered structure at long range.

To deeply investigate the small differences in the structure of materials, the lattice parameters and the unit cell volume of materials were calculated using the Maud software version 2.26.[73,74] The results obtained from the Rietveld refinement for lattice parameters and cell volumes are shown in the Supporting Information, Figure SI-1, and shown in Table 1.

As can be seen in Table 1, the PMO/acac and PMO/PVP unit cell parameters obtained by Rietveld refinement indicate a good agreement with those reported in the literature.[17,21] Moreover, it is possible to observe a slight distortion on the PMO/acac and PMO/PVP structures processed by the hydrothermal method at 100 °C/10 min, especially in the *c* parameter of the PMO/acac system, which can be related to synthesis reactants, i.e., influence of distinct organic composition of modifiers and the experimental hydrothermal conditions adopted. In addition, the distortion of the PMO/acac system can be assigned to the presence of a solvent molecule and/or OH group from the acetylacetone trapped in the crystal lattice.

**4.2. Micro-Raman Spectroscopy.** The group theory calculation presents 26 different vibrations for the $PbMoO_4$, which can be represented by eq 3,[75,76] where all vibrations $A_g$, $B_g$, and $E_g$ are Raman active.

$$\Gamma = 3A_g + 5A_u + 5B_g + 3B_u + 5E_g + 5E_u \quad (3)$$

In materials with scheelite-type structure, the first member of the pairs (g) is a Raman-active mode, and the second member (u) is active only in infrared (IR) frequencies, except for $B_u$ silent modes that are not IR-active. Consequently, 13 zone-center Raman-active modes are expected in $PbMoO_4$, as described by eq 4.[77]

$$\Gamma = 3A_g + 5B_g + 5E_g \quad (4)$$

Figure 2 ((a) PMO/acac and (b) PMO/PVP) shows the Raman spectra in the range from 50 to 1000 $cm^{-1}$ of $PbMoO_4$

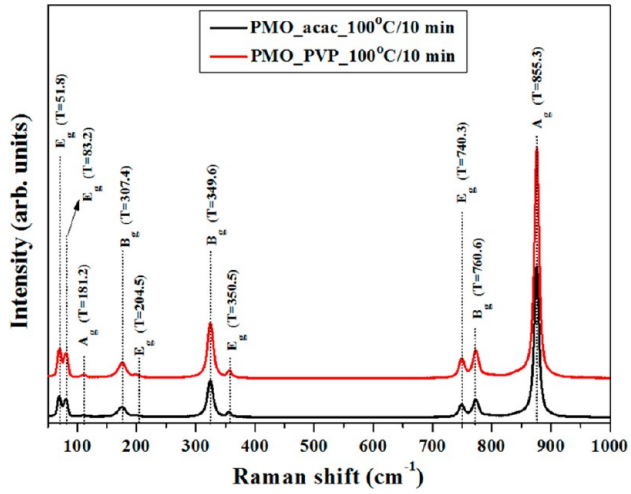


**Figure 2.** Micro Raman spectra in the range from 50 to 1000 $cm^{-1}$ of $PbMoO_4$/acac and $PbMoO_4$/PVP micro-octahedrons processed by the hydrothermal method at 100 °C for 10 min. (T) = Theoretical Raman modes of the triplet state.

samples processed by hydrothermal method at 100 °C/10 min with acetylacetone and polyvinylpyrrolidone, respectively.

According to the literature,[78] it was possible to observe two characteristic vibration groups for molybdate materials. The first vibration mode corresponds to external vibrations, which are related to lattice phonons from the $[PbO_8]$ clusters in fixed cell units. The second belongs to internal vibrations related to the $[MoO_4]$ cluster in the lattice, which are composed of four Raman-active internal modes, $\upsilon_1$ ($A_1$), $\upsilon_2$ ($E_1$), $\upsilon_3$ ($F_2$), and $\upsilon_4$ ($F_2$), one free rotation mode $\upsilon_{f.r.}$ ($F_1$), and one translational mode ($F_2$). As can be seen in Figure 2, the results indicated that all Raman-active modes of PMO/acac (a) and PMO/PVP (b) obtained by the hydrothermal method in this work are

**Table 1. Rietveld Refined Parameters of PMO/acac and PMO/PVP Processed in a Hydrothermal System at 100 °C for 10 min[a]**

| PMO | *a* (Å) | *c* (Å) | *c*/*a* | cell volume (Å$^3$) | $\chi^2$ | R-Bragg (%) | Rwp (%) |
|---|---|---|---|---|---|---|---|
| JCPDS 44-1486 | 5.433 | 12.110 | 2.228 | 357.456 | - | - | - |
| acac 100 °C/10 min | 5.439 | 12.124 | 2.229 | 358.661 | 2.70 | 8.76 | 4.32 |
| PVP 100 °C/10 min | 5.438 | 12.124 | 2.229 | 358.529 | 2.28 | 7.53 | 4.55 |

[a] $\chi^2$, goodness of fit; Rwp, weighted error (%).


dx.doi.org/10.1021/jp407416h | J. Phys. Chem. C 2013, 117, 21382−21395

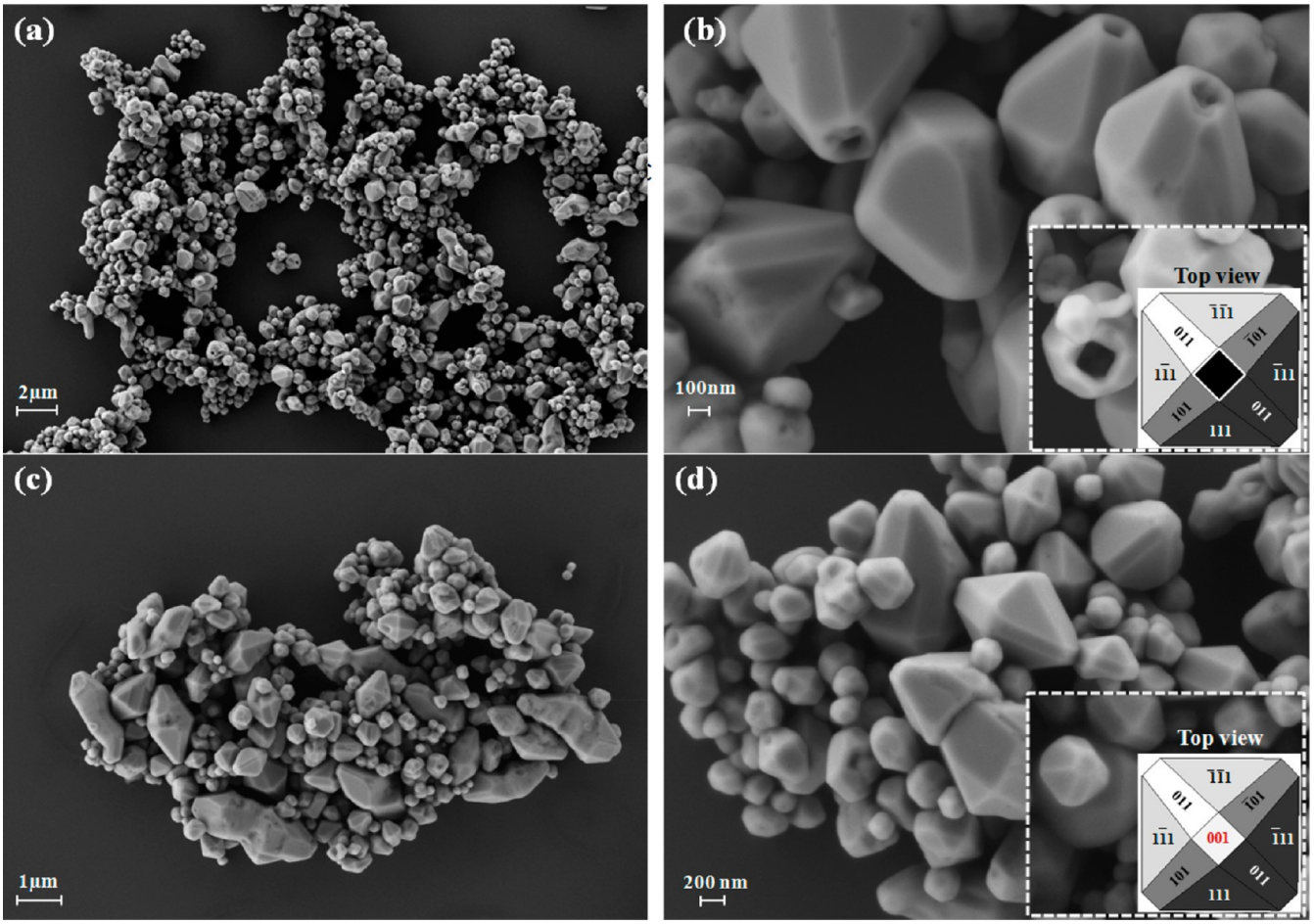


**Figure 3.** FEG-SEM micrographs of $PbMoO_4$ micro-octahedrons processed by the hydrothermal method at 100 °C/10 min: (a,b) PMO/acac and (c,d) PMO/PVP.

characteristic of a tetragonal structure, in agreement with data previously reported in the literature.[25,34,59,79,80] Moreover, the well-defined active-Raman modes suggest that $PbMoO_4$ are structurally ordered at short range, regardless of the different types of modifiers used during hydrothermal synthesis.

Theoretical Raman modes are shown in the low part of Figure 2. They are in agreement with experimental values up to 200 $cm^{-1}$. The modes can be organized in two groups. One group is composed of low-frequency modes with frequencies smaller than 357 $cm^{-1}$, associated to internal bending movements of the $MoO_4$ tetrahedra. The second group is separated from the first group by a phonon gap of about 400 $cm^{-1}$ and is formed by the last three modes associated to Mo−O stretching movements. In relation to experimental Raman modes, there are some differences between these data and those previously published.[81] $B_g$ modes (70 and 197 $cm^{-1}$) now appear at ∼170 and ∼330 $cm^{-1}$, and the $A_g$ mode at 324 $cm^{-1}$ disappears.

First-principle calculations indicate loss of symmetry in achieving the triplet state of $PbMoO_4$ generating a structure with parameters $a$ = 5.326 Å, $b$ = 5.332 Å, $c$ = 5.332 Å and angles $\alpha$ = 90.018°, $\beta$ = 90.004°, $\gamma$ = 90.021°. In the triplet state, a distortion in the surroundings of $[MoO_4]$ and $[PbO_8]$ clusters compared to the fundamental state was observed. One $[MoO_4]$ unit maintains the Mo−O distances at 1.801 Å and angles at 107.4° and 113.8°, while the other increases its value at 1.876 Å and also the distortion with angles of 103.4° and 122.2°. In crystals with the scheelite structure, the indicator of distortion in the surroundings of the tetrahedral anion is the high-frequency $A_g$ vibration, which is the result of the Davydov splitting of the $(A_1)\nu_1$ free tetrahedral anion.[82,83] The $A_g$ mode in the fundamental s state is 314.3 $cm^{-1}$. In passing from the s to t* state, the $A_g$ mode increases to 360.1 $cm^{-1}$. $[PbO_8]$ clusters are also modified, passing to the excited state. Four Pb−O distances of 2.627 Å and four others of 2.639 Å evolve to more distorted clusters with Pb−O distances of 2.519−2.636 Å in one $[PbO_8]$ unit and 2.358−2.598 Å in the other $[PbO_8]$, which form the unit cell. $B_g$ modes in the fundamental state (309.1 $cm^{-1}$) involve Mo−O−Pb motion, which can favor the distortion of $[PbO_8]$ clusters in the t* state (307.4 $cm^{-1}$).

**4.3. FEG-SEM Analysis.** Figures 3(a,b) and 3(c,d) show the FEG-SEM images for the PMO/acac and PMO/PVP micro-octahedrons, respectively. As can be seen, the presence of modifiers, acetylacetone and polyvinylpyrrolidone, has a significant influence on the morphology of lead molybdate powders.

However, Figure 3(a) shows the FEG-SEM image of PMO/acac processed at 100 °C/10 min. A wide homogeneity between micro-octahedrons with well-defined superficial morphology of the material was observed. On the other hand, due to the presence of acetylacetone during the hydrothermal processing, the micro-octahedrons exhibit interesting morphology (Figure 3b). In contrast to a PMO crystal simulated by using the Java Structure Viewer


dx.doi.org/10.1021/jp407416h | J. Phys. Chem. C 2013, 117, 21382−21395

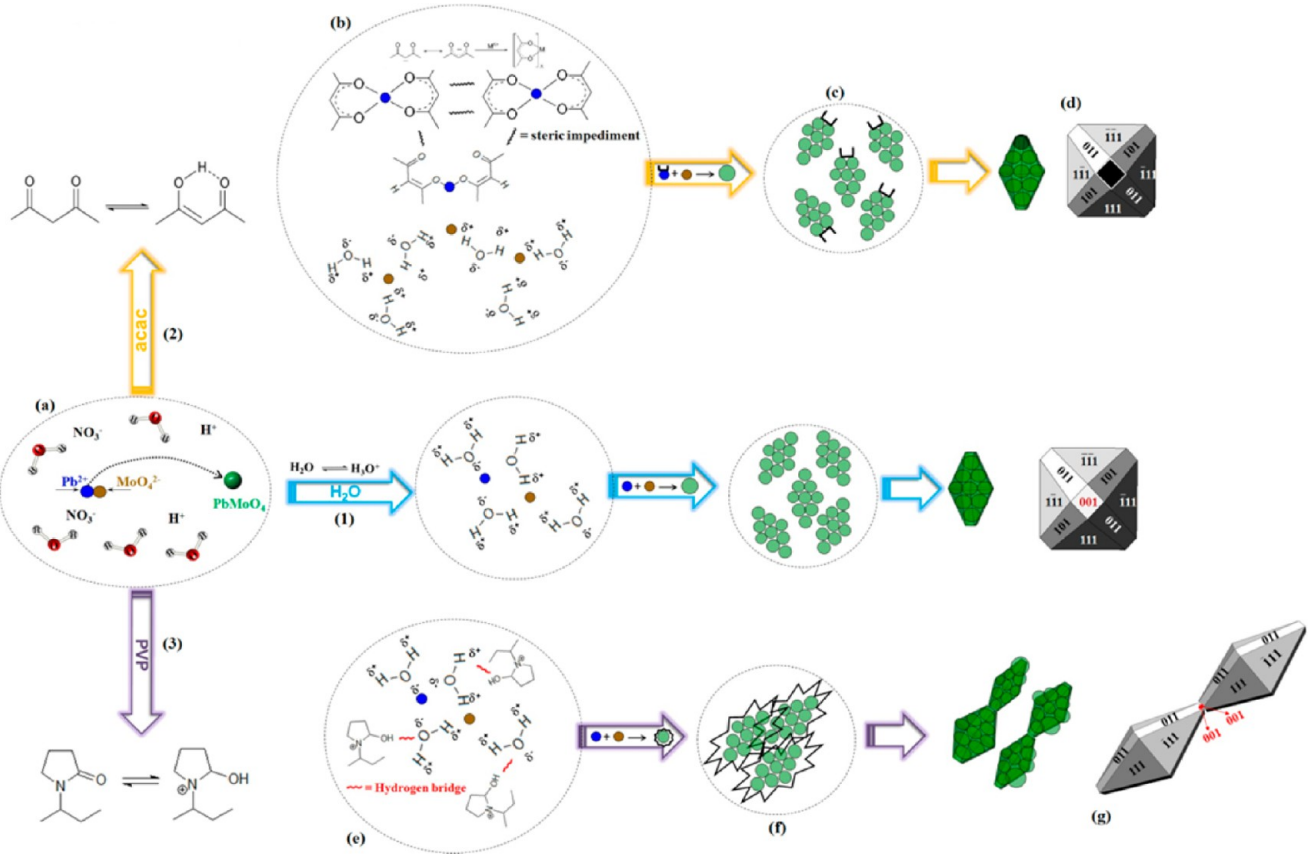


**Figure 4.** Schematic representation of the synthesis and growth mechanism for $PbMoO_4$ crystals by FEG-SEM (1) without modifiers, (2) with acetylacetone (acac), and (3) with polyvinylpyrrolidone (PVP).

Program,[84,85] and according to a previous work,[34] it was found that the growth of the crystallographic plane (001) is not favored in the presence of an acetylacetone chelate modifier.

In principle, few works in the literature have reported that acetylacetone is widely used as a chelating agent to form ligands with metal ions,[86] a stabilizer of ZnO nanoparticles in water as a functionalizing agent,[87] a solvent for solvothermal syntheses of spherical $ZrO_2$,[88] and as a modifier for perovskite thin film.[89] We believe that the formation of a complex between the lead ions and acetylacetone during the hydrothermal synthesis does not favor the growth of the crystallographic plane (001). This mechanism will be discussed later.

Figure 3(c) shows the FEG-SEM image of PMO/PVP processed at 100 °C/10 min. In these conditions, surface defects on micro-octahedron facets are observed, and the coalescence process of the material contributed to the growth of several micro-octahedrons and resulted in an imperfectly oriented attachment mechanism[90,91] between particles, where a crystal growth along [001] is preferred compared to on the [100] direction.[92,93]

Nevertheless, FEG-SEM micrographs were also used to estimate the average particle size distribution of PMO/acac and PMO/PVP micro-octahedrons. The average particle size distribution for micro-octahedrons synthesized by hydrothermal conditions at 100 °C/10 min shows the average particle height of 0.74 $\mu$m and average particle width of 0.60 $\mu$m for the PMO/acac system and 0.55 $\mu$m average particle height and average particle width of 0.48 $\mu$m for the PMO/PVP system (see additional information in Figure SI-2, Supporting Information).

With the use of PVP during the synthesis of PMO micro-octahedrons, the coupling agent promotes the oriented attachment mechanism growth, as shown in Figure 3(c,d). However, the average particle size of PMO/PVP is smaller than that of PMO/acac. This difference in particles sizes arises from the PVP molecules adsorbed onto all PMO surfaces during the reaction making the controllable nucleation and growth of particles, having as a consequence a lower average particle size of PMO.

Compared to PMO/acac micro-octahedrons, the lead acetylacetonate complex does not favor the oriented attachment mechanism or the crystallographic plane (001) as shown in Figure 3(a,b), but micro-octahedrons can grow in the other crystallographic direction due to the absence of a lead acetylacetonate complex in these directions.

**4.4. Growth Mechanism.** Figure 4 illustrates a possible growth mechanism by the effect of acetylacetone and polyvinylpyrrolidone on the shape of micro-octahedral and particle size growth. The growth mechanism will be suggested by the influence of the modifiers on the syntheses of different materials reported in the literature, supported on FEG-SEM micrograph observations.

First, by adding the lead nitrate in contact with molybdic acid in aqueous solution without the presence of any modifier, both ions are free to move in the solution. One can formally consider that the coordination sphere of the water in both ions $Pb^{2+}$ and $MoO_4^{-2}$ is present which causes a fast dissociation of the chemical salts in solution. The positive and negative partial charges of the $H_2O$ are responsible for surrounding the ions, maintaining as close as possible to each other (Figure 4a).


dx.doi.org/10.1021/jp407416h | J. Phys. Chem. C 2013, 117, 21382−21395

However, due to differences in the electronic density between $Pb^{2+}$ and $MoO_4^{2-}$ ions, a strong electrostatic attraction force occurs between both, resulting in the formation of the first $PbMoO_{4(s)}$ precipitate. Second, the precipitation rate increased by the addition of 5 mL of $NH_4OH$ (pH = 11) into this solution. When one of these suspensions was processed by hydrothermal conditions, it was possible to note an increase in the $PbMoO_4$ crystal size and also to detect all facets of the micro-octahedral particles, including the 001 face, as reported in a previous work.[34]

In the case of acetylacetone, there is a tautomeric equilibrium between keto and enol forms in solution, where the keto shape is in equilibrium with the cyclic enol form. The acetylacetone behaves mainly as a bidentate $O^-$ donor ligand, forming six-membered chelantes with numerous metal ions, including the $Pb^{2+}$ ion (Figure 4(b)).

When acetylacetone is added to the reaction medium, it behaves like a weak acid. The anion resulting from this ionization, acetylacetonate, can act as a ligand for metal ions. The coordination of the deprotonated enol form, the acetylacetonate ion ($accac^-$), to metal cations usually results in neutral complexes, which in the case of $Pb^{2+}$ results in a complex with square pyramid geometry ($Pb(accac)_2$). We believe that the complex geometry of $Pb(accac)_2$ significantly contributed to the evolution of the new morphology observed for the synthesis of PMO/acac powders. The complex played a role in the inactivation through a steric layer, which is the case of the acetylacetonate structure (Figure 4(c)), which in turn has favored inhibition of the specific crystallographic plane [001] (Figure 4(d)) at the time of nucleation and formation of $PbMoO_4$ micro-octahedra, during the hydrothermal process at 100 °C/10 min.

On the other hand, the use of a polyvinylpyrrolidone coupling agent to control the morphology of the $PbMoO_4$ also revealed morphological changes of the material. Polyvinylpyrrolidone is extensively used as the stabilizer and structure-directing agent in nanotechnology due to its excellent adsorption ability and solubility in water.

In the case of PVP, its presence during the reaction promoted an increase in the viscosity of the reaction medium, which plays the role of decreasing the spontaneous interaction between $Pb^{2+}$ and $MoO_4^{2-}$ ions, even under hydrothermal processing conditions for 10 min at 100 °C (Figure 4(e)). We believe that as a consequence of the use of polyvinylpyrrolidone a slow rate of formation (nucleation) and aggregation of several microcrystals take place in the system, promoting the formation of the $PbMoO_4$ micro-octahedra (Figure 4(f)) by coalescence, which contributes to the growth of distorted and disordered micro-octahedra by the growth mechanism of a crystallographic orientation mechanism (Oriented Attachment) (Figure 4(g) and additional information in Figure SI-3, Supporting Information).

*Surfaces and Growth Mechanism.* Since many types of metal oxides form a wide range of oxygen-deficient intermediate phases,[95−97] it is generally believed that the reconstruction of the metal oxide surface is related to an ordered oxygen vacancy type defect.[97,98] The analysis of different Pb and Mo arrangements in different planes leads to diverse degrees of broken chemical bonds on their surface and sites. While bonds and coordination in the core interior retain their bulk nature, i.e., $MoO_4$ and $PbO_8$, in the surface undercoordinated Pb is found. The electronic structure of $PbMoO_4$ surfaces has scarcely been studied. Table 2 presents the calculated surface energy values ($E_{surf}$) for (001), (100), (110), (101), and (111) facets, the number of $PbMoO_4$ layers of each surface model, and their calculated band gap energy. Figure 5 shows the resulting geometry of optimized surfaces.

**Table 2. Number of $PbMoO_4$ Units, Area, Surface Energy, and Band Gap Energy for (001), (100), (110), (101), and (111) Surfaces of $PbMoO_4$[a]**

| | $n$ | area (Å$^2$) | $E_{surf}$ (J·m$^{-2}$) | relax (%) | $E_{gap}$ (eV) |
|---|---|---|---|---|---|
| bulk | 2 | | | | 3.70 |
| [001] | 5 | 30.07 | 0.28 | 33.2 | 3.58 |
| [100] | 8 | 66.84 | 0.37 | 63.8 | 3.99 |
| [110] | 5 | 47.26 | 0.58 | 75.5 | 3.61 |
| [101] | 4 | 36.65 | 0.66 | 64.8 | 3.86 |
| [111] | 10 | 99.20 | 0.61 | 60.4 | 3.60 |

[a]All surfaces are O-terminated.

In the (001) surface, Pb is surrounded by six O atoms, with three sets of two equivalent distances 2.43, 2.50, and 2.72 Å, respectively. The (100) surface shows a Pb coordinated to five O atoms at distances 2.23 (×2), 2.31, 2.89, and 2.92 Å, respectively. In the (110) and (111) surfaces, Pb is surrounded by only four O atoms at a range of distances 2.17−2.87 Å and 2.26−2.92 Å, respectively. Mo atoms have a tetrahedral environment in all surfaces more distorted than in bulk, with clearly two different distances, 1.75 and 1.86 Å in (001); 1.71 and 1.79 Å in (100); and 1.74 and 1.87 Å in (110), respectively. Therefore, undercoordination at the Pb atom can explain the stability order of surface energy between surfaces since the lack of three or four O atoms in (100) or (110) and (111) facets, respectively, induces more distortions than the deficiency of two O atoms in (001) facets.[32] In the case of the (101) facet, Pb atoms are located far from the top of the surface and are coordinated to six O atoms (in the range 2.32−2.94 Å). Figure 6 shows the resulting Wulff construction derived from calculated surface energy values[94] for different crystalline planes. Although theoretical calculations predict a low percentage of (100) and (110) facets in the resulting morphology, both experimental and theoretical results point out that a crystal growth along the [001] crystal direction is preferred to the [100] direction for $PbMoO_4$. A growth combination along the [001] direction may lead to the formation of octahedron-like $PbMoO_4$ microcrystals with small exposed (001) facets at the top and bottom of the octahedron-like microcrystals.[34]

The second surface in order of stability is (100) (see Table 2), and therefore it appears in the Wulff construction (Figure 6) obtained from the computed surface energies. Although the (100) surface is not experimentally seen, it has a small extent in equilibrium morphologies reported in the literature.[95]

**4.5. UV−vis Absorption Spectroscopy Analyses.** The UV−vis absorbance spectra of PMO/acac and PMO/PVP micro-octahedrons synthesized at 100 °C for 10 min was used to understand how the hydrothermal processing can intorduce intermediate energy levels within the band gap of these materials. Wood and Tauc[96] proposed a method to estimate the optical band gap energy ($E_{gap}$), which is associated with absorbance and photon energy by the following equation.

$$h\nu\alpha \propto (h\nu - E_{gap})^n \quad (5)$$

where $\alpha$ is the absorbance; $h$ is the Planck constant; $\nu$ is the frequency; $E_{gap}$ is the optical band gap; and $n$ is a constant associated with the different types of electronic transitions ($n$ =


dx.doi.org/10.1021/jp407416h | J. Phys. Chem. C 2013, 117, 21382−21395

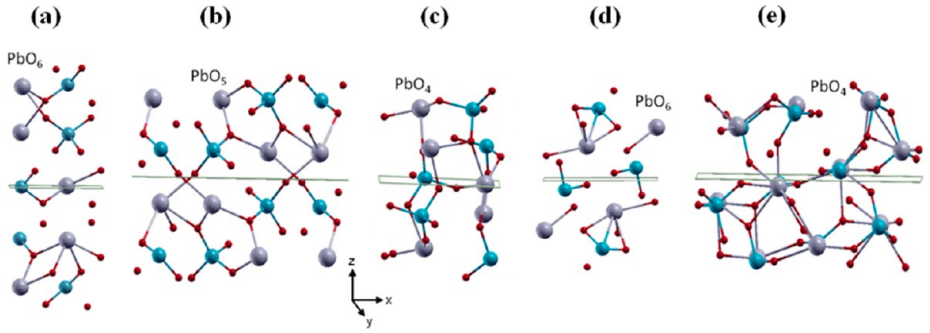


**Figure 5.** Geometry of optimized surfaces (a) (001), (b) (100), (c) (110), (d) (101), and (e) (111).

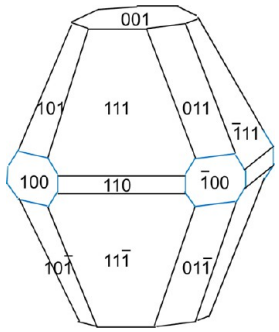


**Figure 6.** Wulff constructed nanocrystal using SOWOS code.[94]

1/2, 2, 3/2, or 3 for direct allowed, indirect allowed, direct forbidden, and indirect forbidden transitions, respectively). According to Lacomba-Perales[97] et al. and a previous report,[34] molybdates with scheelite-type tetragonal structure present direct allowed electronic transition, i.e., $n$ equal to 1/2. The band gap was estimated using eq 3, and the results obtained are listed in Table 3, which can be compared with $E_{gap}$ values

**Table 3. Comparative Results between the $E_{gap}$ Values of $PbMoO_4$ Obtained in This Work and Those Reported in the Literature by Different Synthesis Methods**

| method | temperature (°C) | time (min) | $E_{gap}$ (eV) | ref |
|---|---|---|---|---|
| reflux method | | 1440 | 3.31 | 37 |
| hydrothermal | 180 | 1440 | 3.21 | 24 |
| coprecipitation/thermal treatment | 350 | 1440 | 3.16 | 99 |
| solid-state reaction | 950 | 4320 | 3.1 | 20 |
| solvothermal | 160 | 720 | 3.3 | 12 |
| hydrothermal/acac | 100 | 10 | 3.05 | this work |
| hydrothermal/PVP | 100 | 10 | 3.17 | this work |

recently reported in the literature. Our research group synthesized the hierarchical assembly of $CaMoO_4$ nano-octahedrons, and their photoluminescence properties and structural order−disorder effect as a function of the particle/region size[98] have been studied. This work analyzes the structure order−disorder using theoretical models and concludes that geometric distortions along the $y$ and $z$ planes of the scheelite structure affect the order−disorder in the lattice, which causes the appearance of intermediate energy levels within the band gap.

In Figure SI-4 (Supporting Information), the PMO/acac and PMO/PVP band gap values were 3.05 and 3.17 eV, respectively. We can observe the result of the refinement Rietveld method (Table 1) that the structure parameters of PMO/PVP are closer to the reference used in the work (JCPDS 44-1486) than PMO/acac. Therefore, the increase in structural organization leads to a reduction in these intermediary energy levels, increasing the $E_{gap}$ values. The presence of disorder structure of PMO/acac due to increased defects in the lattice (tetrahedral and octahedral distortion) favors the decrease in the bad gap, which can be directly related to increased defects, such as the absence of the (001) face on the micro-octahedron morphology (Figure 3d), which raises the local levels within the band gap region, reducing the optical band gap measure.

**4.6. Photocatalytic Activity of $PbMoO_4$.** Recently, several studies have investigated the photocatalytic degradation properties of $PbMoO_4$ of different types of organic dyes. For this purpose, different synthesis routes have been proposed to obtain new structural morphologies and particle size, to improve the photocatalytic properties.[55−57,99−101]

In this work, with the aid of different modifiers, it was possible to modify the morphology and create defects on the surface and $PbMoO_4$ clusters, as can be seen in Figures 3b and 3d. To demostrate the photocatalytic activity of PMO/acac and PMO/PVP materials obtained by hydrothermal synthesis at 100 °C/10 min, photodegradation of RhB dye was carried out in aqueous dispersion (RhB + PMO/acac or PMO/PVP) under UV lamps with maximum intensity at 254 nm. The temporal evolution of adsorption and photocatalytic degradation of aqueous RhB dye solution ($C_n/C_o$) is shown in Figure 7. To observe the influence of acetylacetone and polyvinylpyrrolidone on the $PbMoO_4$ micro-octahedron morphology, a similar experiment for $PbMoO_4$ micro-octahedrons without any modifier addition (PMO/WS) was carried out. The structural, morphological, and optical characterization of these micro-octahedrons can be seen in our previous work.[34] As can be seen in Figure 7(a), for PMO/WS micro-octahedrons, the RhB dye was totally photodegraded after 55 min under UV light illumination. The result indicates that even without any modification on the $PbMoO_4$ morphology the RhB photodegradation efficiency is high. On the other hand, for the synthesized PMO/acac and PMO/PVP materials (Figure 7(b) and (c), respectively), the photodegradation rate of RhB dye was higher than PMO/WS due to the action of modifiers, which promoted remarkable changes on the $PbMoO_4$ morphology, having as a consequence the formation of surface defects and distortions in $[MoO_4]$ or $[PbO_8]$ clusters. The degradation degree of the RhB dye increased when $PbMoO_4$


dx.doi.org/10.1021/jp407416h | J. Phys. Chem. C 2013, 117, 21382−21395

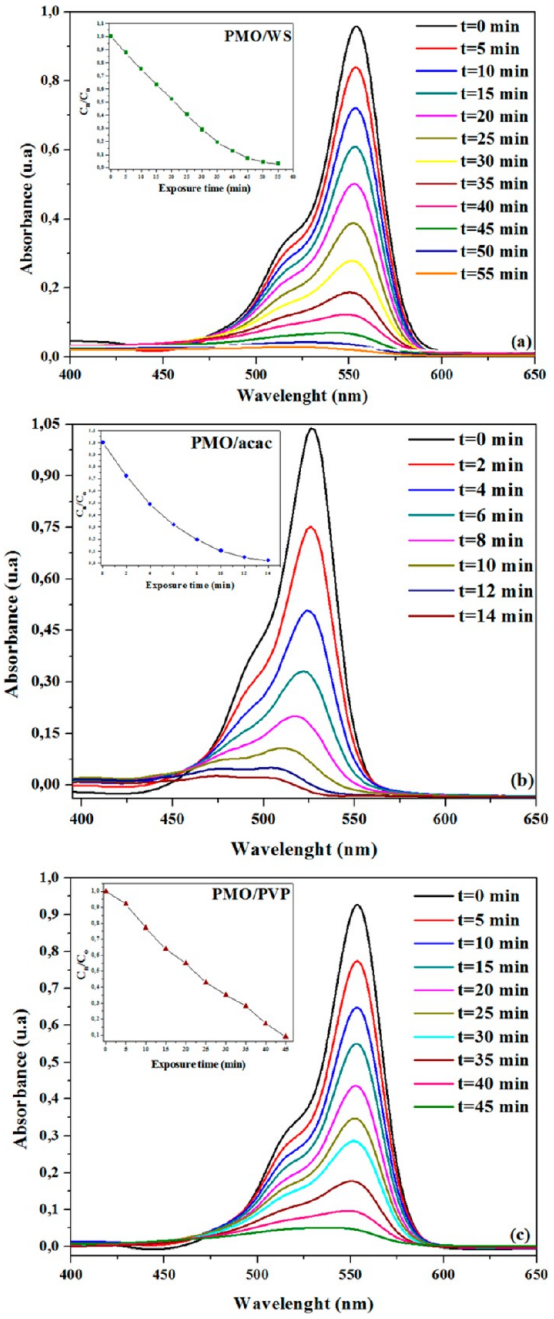


**Figure 7.** UV−vis absorption spectra for (a) PMO/WS, (b) PMO/acac, and (c) PMO/PVP micro-octahedrons during different exposure times of illumination for the photodegradation of RhB dye. Inset shows photodegradation efficiencies of RhB as a function of irradiation time for different photocatalysts.

was synthesized by a hydrothermal process at 100 °C/10 min with a polyvinylpyrrolidone coupling agent (Figure 7(c)), where the RhB dye was totally photodegraded after 45 min under UV light illumination. According to the literature, a scheelite-type structure tends to be faceted and aligned by "docking" processes involving crystallographic fusion between some faces with lower surface energy because they are more abundant and generate an extended morphology.[31] Figure 3(c) and Figure SI-3(c,d) (Supporting Information) show the growth process of these morphologies through a self-organization of adjacent microcrystals in a similar crystallographic orientation ("oriented attachment"). The growth along the [001] direction promoted the aggregation of several particles on similar crystallographic orientations, favoring the coalescence of $PbMoO_4$ micro-octahedrons, which promote more potential active sites on the surface (defects), in relation to PMO/WS for RhB dye photodegradation.

For PMO/acac materials, different morphologies compared to PMO/WS and PMO/PVP were observed. Recently, Shen et al.[54] synthesized $PbMoO_4$ microcrystals with preferentially exposed (001) facets by a facile surfactant-assisted hydrothermal process in the presence of cetyltrimethylammonium bromide (CTAB), which exhibited higher catalytic activity compared to the (110) facet. Similarly, Hashim et al.[55] produced $PbMoO_4$ dendrites with exposure on the (001) facet with photocatalytic thorough degradation of rhodamine B.

In our work, it was observed that the absence of the (001) facet exhibited enhanced activity for the RhB photodegradation instead of exposing it. As can be seen in Figure 7(b), the complete degradation of the RhB dye was achieved in only 14 min of exposure to UV light, demonstrating the high catalytic properties of $PbMoO_4$ in the absence of the (001) face in the material structure, as shown in Figure 3(b). In our research group, a model based on complex clusters was proposed to explain the photocatalytic activity of the $SrWO_4$ microcrystal due to the photo-oxidation of RhB.[102] For $PbMoO_4$ synthesized by the hydrothermal method at 100 °C/10 min with acetylacetone, we believe that the $PbMoO_4$ catalyst without the presence of the (001) facet has a higher ability to generate $e'-h^{\bullet}$ pairs due to defects on the specific surface (001), providing a fast degradation of the RhB dye.

The cluster-like elucidation of the photocatalytic performance is supported and strengthened by different extrinsic (surface) and intrinsic (bulk) defect distributions. The defect structure and density variation surface and/or bulk might be responsible for the different photocatalytic behavior of $PbMoO_4$. Effective charge separation (electron/hole) requires the presence of a cluster-to-cluster charge transfer (CCCT) of electrons or holes from $[MoO_4]^x_o/[MoO_4]^x_d$ or $[PbO_8]^x_o/[PbO_8]^x_d$. One way to boost photocatalyst efficiency is to exchange ordered complex clusters to disordered complex clusters. Consequently, the effect of surface properties on the photocatalytic performance should be considered in terms of $[MoO_4]^x_o$ and $[PbO_8]^x_o$ clusters and $[MoO_4]^x_d$ and $[PbO_8]^x_d$ clusters, where o = order and d = disorder.

The first effect is intrinsic to the $PbMoO_4$ material and is derived from the bulk/surface material composed of an asymmetric distorted $[MoO_4]_d$ or $[PbO_8]_d$ and ordered $[MoO_4]_o$ or $[MoO_4]_o$. The ordered complex cluster often behaves as an electron sink and improves the charge separations within the semiconductor photocatalytic system. These electron polarons can then be discharged to acceptors ($O_2$) at the interface with a relatively lower over reduction potential. Consequently, the effect of surface properties on the photocatalytic activity should be considered in terms of the following reactions

$$[MoO_4]^x_o + [MoO_4]^x_d \xrightarrow{h\nu} [MoO_4]'_o + [MoO_4]^{\bullet}_d \quad (6)$$

$$[PbO_8]^x_o + [PbO_8]^x_d \xrightarrow{h\nu} [PbO_8]'_o + [PbO_8]^{\bullet}_d \quad (7)$$

Upon the adsorption of a photon with energy equal to or greater than the band gap of the semiconductor, an electron polaron/hole pair is generated in the bulk/surface. These charge carriers migrate toward the catalytic surface where the


dx.doi.org/10.1021/jp407416h | J. Phys. Chem. C 2013, 117, 21382−21395

charge transfer between the perfect or defective surface and adsorbed oxygen molecules produces several kinds of charged species including the $O_2'$ superoxide ion. The molecular oxygen reactivity with $[MoO_4]$ or $[PbO_8]$ results in the following species

$$[MoO_4]_d^{\bullet} + O_2 \xrightarrow{h\nu} [MoO_4]_d^{\bullet}\cdots O_{2(ads)} \quad (8)$$

$$[MoO_4]_d^{\bullet}\cdots O_{2(ads)} + [MoO_4]_o' \xrightarrow{h\nu} [MoO_4]_d^{\bullet}\cdots O_{2(ads)}' + [MoO_4]_o^{x} \quad (9)$$

$$[PbO_8]_d^{\bullet} + O_2 \xrightarrow{h\nu} [PbO_8]_d^{\bullet}\cdots O_{2(ads)} \quad (10)$$

$$[PbO_8]_d^{\bullet}\cdots O_{2(ads)} + [PbO_8]_o' \xrightarrow{h\nu} [PbO_8]_d^{\bullet}\cdots O_{2(ads)}' + [PbO_8]_o^{x} \quad (11)$$

The clusters formed by the complex $PbMoO_4$ cluster interact with water and separate it into its hydroxyl radicals and hydrogen ions according to the following reactions

$$[MoO_4]_d^{\bullet} + H_2O \xrightarrow{h\nu} [MoO_4]_d^{\bullet}\cdots OH^* + H^{\bullet} \quad (12)$$

$$[PbO_8]_d^{\bullet} + H_2O \xrightarrow{h\nu} [PbO_8]_d^{\bullet}\cdots OH^* + H^{\bullet} \quad (13)$$

The primary products of the partial oxidation reaction between water and a complex cluster $[MoO_4]_d^{\bullet}$ or $[PbO_8]_d^{\bullet}$ are hydroxyl radicals, OH*. These radicals exhibit high oxidation power and produce mineralization of an organic compound in water. The primary reaction is the formation of superoxide species $[MoO_4]_d^{\bullet}\cdots O_2'$ or $[PbO_8]_d^{\bullet}\cdots O_2'$. These species then react with the hydrogen ion $H^{\bullet}$ and form a hydrogen peroxide radical ($O_2H^*$) according to the following reactions

$$[MoO_4]_d^{\bullet}\cdots O_{2(ads)}' + H^{\bullet} \rightarrow [MoO_4]_d^{\bullet}\cdots O_2H^* \quad (14)$$

$$[PbO_8]_d^{\bullet}\cdots O_{2(ads)}' + H^{\bullet} \rightarrow [PbO_8]_d^{\bullet}\cdots O_2H^* \quad (15)$$

OH* and $O_2H^*$ radicals react with an organic compound and ultimately cause their oxidation. The nature of superoxide radicals can be described using a complex cluster where the polaron/hole polaron electron exchanges from structural disorder to structural order to absorb molecular oxygen and water molecular oxygen and water.

Finally, it is noteworthy that it is still challenging to correlate the surface defects with the photocatalytic activity. A major problem is that the defects are interacting with many other factors and the photocatalytic activity of $PbMoO_4$ can be dominated by the balance between all these factors. One should keep in mind that defects exist in most $PbMoO_4$ samples except perfect single crystals, and the degrees of defects may differ greatly in different samples. Therefore, it is almost impossible to exclude the effects of defects on the photocatalytic activity of $PbMoO_4$ when studying the effects from other factors, e.g., crystalline phases and exposed crystal facets, while it is rational to investigate the sole effect of defects on the photocatalytic activity of $PbMoO_4$, providing that other factors could be kept unchanged.

**4.7. Electronic Structure of Bulk Ground and Triplet Sates and Surfaces.** Figure 8(a) shows the band structure and DOS projected on atoms for the triplet structure. The distortion process on the fundamental $[MoO_4]_d$ and $[PbO_8]_d$ clusters to the excited $[MoO_4]_d^*$ and $[PbO_8]_d^*$ tetrahedral and

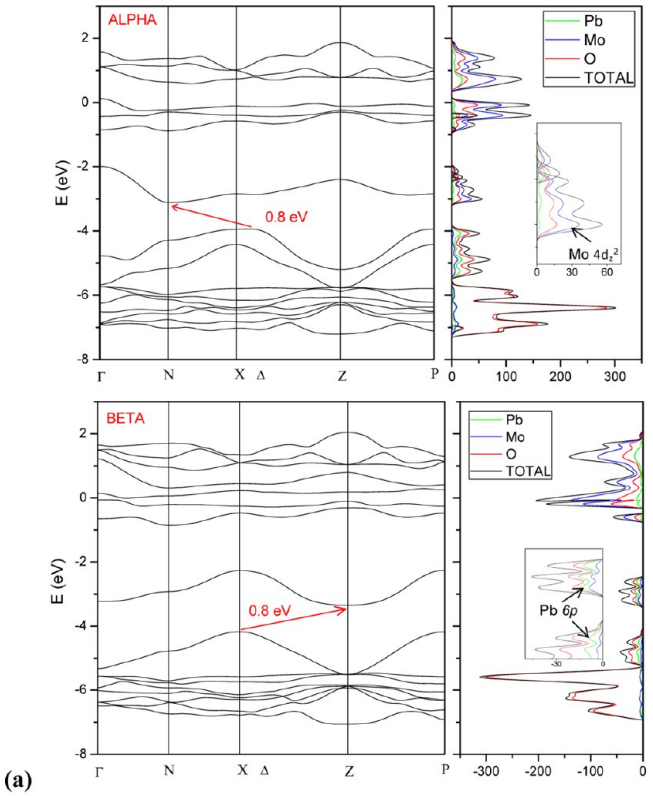


(a)

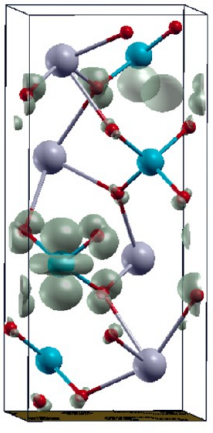

(b)

**Figure 8.** Calculated band structure and total DOS projected on atoms of triplet PMO (a) and the spin charge density location in the unit cell of triplet PMO (b).

deltahedral groups, respectively, favors the formation of intermediary energy levels in the conduction band (CB) conferring conductor properties to this material. In the ground state, the top of the valence band (VB) is located on the Δ point, and the bottom of the conduction band (CB) is on point N, presenting an indirect band gap of 3.69 eV.[81] Zhang et al. investigated in detail the electronic band structures of crystalline $PbWO_4$, $PbMoO_4$, $CaWO_4$, and $CaMoO_4$ scheelites, by means of linearized augmented plane-wave calculations.[103] An analysis of DOS projected on atoms and orbitals shows that the maximum valence band (VB) is derived mostly from O 2p orbitals for fundamental and excited states. The CB in the fundamental state is composed of Mo $4d_{xy}$ over $4d_{z^2}$ in the first


dx.doi.org/10.1021/jp407416h | J. Phys. Chem. C 2013, 117, 21382−21395

set of CBs and by $4d_{x^2-y^2}$ in the second CB. In the triplet state, it appears that new energy levels are lower in energy previous to this first CB composed by Mo_2 $4d_{z^2}$ orbitals which form more $[MoO_4]$ distorted clusters, as can be seen in the alpha band structure. Some other intermediate levels appear in the uppermost of the VB in the beta band structure, mostly derived from Pb 6p orbitals. Figure 8(b) shows the spin density charge, which is mostly accumulated in Mo_2 $4d_{z^2}$ orbitals, so there is a charge transfer from O 2p orbitals to empty Mo_2 $4d_{z^2}$ orbitals. The rest of the CB is found to be governed by Mo $4d_{x^2-y^2}$.

Therefore, an analysis of site- and orbital-resolved DOS shows a significant dependence of the Mo CB DOSs on local coordination. During the excitation process, some electrons are promoted more feasibly from the oxygen 2p states to these molybdenum 4d states ($4d_{z^2}$) through the absorption of photons. The emission process of photons occurs when an electron localized in the molybdenum 4d state moves into an empty oxygen 2p state.

The band structure and DOS projected on atoms for singlet and triplet surfaces have also been obtained, and as in the bulk, the formation of intermediary energy levels between CV and CB is favored by the distortion on $[MoO_4]_d$ and $[PbO_8]_d$ clusters. In particular, the (001) triplet surface shows a Pb coordinated to six O atoms at distances of 2.40 (×2), 2.42 (×2), and 2.65 (×2) Å. The spin density is concentrated around the Mo2 atom, which forms the more distorted $[MoO_4]_d$ clusters, with the same angles as in the bulk and two distances Mo−O of 1.924 Å and another two of 1.835 Å. Such distortion can favor the absence of the (001) facet, and then the growth along the [001] direction may lead to the formation of octahedron-like $PbMoO_4$ microcrystals without the presence of exposed (001) facets.

Therefore, the action of acetylacetone and polyvinylpyrrolidone on the $PbMoO_4$ system would be comparable to the localization of an excited state, having as a consequence the formation of surface defects and distortions in $[MoO_4]$ or $[PbO_8]$ clusters, which promote remarkable changes on the $PbMoO_4$ morphology.

## 5. CONCLUSIONS

In summary, unique $PbMoO_4$ powders with predominant (111), (100), (011), and (110) facets have been prepared using coprecipitation and hydrothermal methods in the presence of acetylacetone or polyvinylpyrrolidone with a good control of the synthesis parameters. $PbMoO_4$ crystals were characterized by X-ray diffraction (XRD), micro-Raman (MR) spectroscopy, field-emission gun scanning electron microscopy (FEG-SEM), and ultraviolet visible absorption spectroscopy (UV−vis). The photocatalytic efficiency of powder suspensions of $PbMoO_4$ micro-octahedrons without the presence of a (001) surface exhibits enhanced activity for the photodegradation of rhodamine B (RhB) under ultraviolet−visible light irradiation. The surface/bulk defects can influence the separation of photogenerated electron−hole pairs on $PbMoO_4$ under irradiation and, therefore, influence the activity in photocatalytic reaction. There is a direct relationship between the surface specific photocatalytic activity and the surface/bulk defect. The photocatalytic superiority of this material should be synergistically attributed to its high crystallinity and oriented subunit alignment as well as exposed high-energy (111), (100), (011), and (110) facets. The detailed comparison with experimental data shows the high degree of agreement, and thus we are confident that our findings can provide useful information and can serve as a guideline for rational design of $PbMoO_4$-based materials for various catalytic applications.

## ■ ASSOCIATED CONTENT

### Supporting Information

Figures SI-1−SI-4. This material is available free of charge via the Internet at http://pubs.acs.org.

## ■ AUTHOR INFORMATION

### Corresponding Author

*Tel.: +55-84-3342-2260. Fax: +55-84-3342-2406. E-mail: mauricio.bomio@ct.ufrn.br.

### Notes

The authors declare no competing financial interest.

## ■ ACKNOWLEDGMENTS

The authors thank the financial support from the following Brazilian research financing institutions: CNPq, FAPESP, CAPES, RECAM (Rede de Pesquisa em Catalisadores Ambientais) processo nº 564913/2010-3; MCT/CNPq no 74/2010 and Universal 14/2011 processo nº 481288/2011-2, and nº 150753/2013-6 National Council for Scientific and Technological Development (CNPq), Prometeo/2009/053 (Generalitat Valenciana) and Ministerio de Economía y Competitividad (Spain), CTQ2012-36253-C03-02, and the Spanish−Brazilian program (PHB2009-0065-PC) for their financial support.

## ■ REFERENCES

(1) Mikhailik, V. B.; Kraus, H. Performance of Scintillation Materials at Cryogenic Temperatures. *Phys. Status Solidi B.* **2010**, *247*, 1583−1599.

(2) Mikhailik, V. B.; Kraus, H.; Kapustyanyk, V.; Panasyuk, M.; Prots, Y.; Tsybulskyi, V.; Vasylechko, L. Structure, Luminescence and Scintillation Properties of the $MgWO_4$ −$MgMoO_4$ System. *J. Phys.: Condens. Matter* **2008**, *20*, 365219−36524.

(3) Ahmad, G.; Dickerson, M. B.; Church, B. C.; Cai, Y.; Jones, S. E.; Naik, R. R.; King, J. S.; Summers, C. J.; Kröger, N.; Sandhage, K. H. Room-Temperature Formation of Crystalline Calcium Molybdate Phosphor Microparticles via Peptide-Induced Precipitation. *Adv. Mater.* **2006**, *18*, 1759−1763.

(4) Sen, A.; Pramanik, P. A Chemical Synthetic Route for the Preparation of Fine-Grained Metal Molybdate Powders. *Mater. Lett.* **2002**, *52*, 140−146.

(5) Guo, C.; Xu, J.; Wang, S.; Li, L.; Zhang, Y.; Li, X. Facile Synthesis and Photocatalytic Application of Hierarchical Mesoporous $Bi_2MoO_6$ Nanosheet-Based Microspheres. *Cryst. Eng. Comm.* **2012**, *14*, 3602−3608.

(6) Duan, F. Z.; Yan, C.; Ming, Q. Enhanced Photocatalytic Activity of Bismuth Molybdate via Hybridization with Carbon. *Mater. Lett.* **2011**, *65*, 191−193.

(7) Mai, L.-Q.; Yang, F.; Zhao, Y.-L.; Xu, X.; Xu, L.; Luo, Y.-Z. Hierarchical $MnMoO_4$/$CoMoO_4$ Heterostructured Nanowires with Enhanced Supercapacitor Performance. *Nat. Commun.* **2011**, *2*, 1−5.

(8) Li, H. C.; Si, W. D.; Wang, R. L.; Xuan, Y.; Liu, B. T.; Xi, X. Dielectric Properties of $SrTiO_3$ Thin Films Grown on Various Perovskite Electrodes by Pulsed Laser Deposition. *Mater. Sci. Eng., B* **1998**, *56*, 218−222.

(9) Ding, Y.; Yu, S. H.; Liu, C.; Zang, Z. A. 3D Architectures of Iron Molybdate: Phase Selective Synthesis, Growth Mechanism, and Magnetic Properties. *Chem.—Eur. J.* **2007**, *13*, 746−753.

(10) Achary, S. N.; Patwe, S. J.; Mathews, M. D.; Tyagi, A. K. High Temperature Crystal Chemistry and Thermal Expansion of Synthetic

Powellite ($CaMoO_4$): A High Temperature X-ray Diffraction (HT-XRD) Study. *J. Phys. Chem. Solids* **2006**, *67*, 774−781.
(11) Sun, Y.; Li, C.; Wang, L.; Ma, X.; Zhang, Z.; Song, M.; Ma, P. Synthesis of $SrMoO_4$ Microstructures by the Microwave Radiation-Assisted Chelating Agent Method. *Cryst. Res. Technol.* **2011**, *46*, 973−978.
(12) Alves, H.; Hofstaetter, A.; Leiter, F.; Meyer, B. K.; Romanov, N. G.; Novotny, R.; Korzhik, M. V. Green Emitting Molybdate Complexes in $PbWO_4$ - Results of an ODMR Study. *Radiat. Meas.* **2001**, *33*, 641−644.
(13) Zhen, L.; Wang, W. S.; Xu, C. Y.; Shao, W. Z.; Ye, M. M.; Chen, Z. L. High Photocatalytic Activity and Photoluminescence Property of Hollow $CdMoO_4$ Microspheres. *Scr. Mater.* **2008**, *58*, 461−464.
(14) Groenink, J. A.; Blasse, G. Some New Observation on the Luminescence of $PbMoO_4$ and $PbWO_4$. *J. Solid State Chem.* **1980**, *32*, 9−20.
(15) Senguttuvan, N.; Babu, S. M.; Subramanian, C. Synthesis, Crystal Growth and Mechanical Properties of Lead Molybdate. *Mater. Sci. Eng., B* **1997**, *47*, 269−273.
(16) Tyagi, M.; Sangeeta; Desai, D. G.; Sabharwal, S. C. New Observations on the Luminescence of Lead Molybdate Crystals. *J. Lumin.* **2008**, *128*, 22−26.
(17) Errandonea, D. M.; Manjón, F. J.; Santamaria-Perez, D.; Grover, V.; Achary, S. N.; Tyagi, A. K. High-Pressure X-Ray Diffraction Study of Bulk and Nanocrystalline $PbMoO_4$. *J. Appl. Phys.* **2010**, *108*, 073518−073523.
(18) Spassky, D. A.; Ivanov, S. N.; Kolobanov, V. N.; Mikhailin, V. V.; Zemskov, V. N.; Zadneprovski, B. I.; Potkin, L. I. Optical and Luminescent Properties of the Lead and Barium Molybdates. *Radiat. Meas.* **2004**, *38*, 607−610.
(19) Piwowarska, D.; Kaczmarek, S. M.; Berkowski, M. Dielectric, Optical and EPR Studies of $PbMoO_4$ Single Crystals, Pure and Doped with Cobalt Ions. *J. Non-Cryst. Solids* **2008**, *354*, 4437−4442.
(20) Bernhardt, H.; Schnell, R. Modulation-Spectroscopic Investigations of Defect Centres in $PbMoO_4$ Crystals. *Phys. Status Solidi A* **1981**, *64*, 207−214.
(21) Hofstaetter, A.; Oeder, R.; Scharmann, A.; Schwabe, D.; Vitt, B. Paramagnetic Resonance and Thermoluminescence of the $PbWO_4$/$PbMoO_4$ Mixed Crystal System. *Phys. Status Solidi B* **1978**, *89*, 375−380.
(22) Neimann, A. Y.; Afanasiev, A. A.; Feodorova, L. M.; Gabrielian, V. T.; Karagezian, S. M. Deviation from Stoichiometry and Electron Transfer in $PbMoO_4$. *Phys. Status Solidi A* **1984**, *83*, 153−158.
(23) Bollmann, W. Coloration, Photoconductivity, Photo and Thermoluminescence of $PbMoO_4$ Crystals. *Krist. Tech.* **1980**, *15*, 367−375.
(24) Kudo, A.; Steinberg, M.; Bard, A.; Campion, A.; Fox, M.; Mallouk, T.; Webber, S.; White, J. Photoactivity of Ternary Lead-Group IVB Oxides for Hydrogen and Oxygen Evolution. *Catal. Lett.* **1990**, *5*, 61−66.
(25) Zverev, P. G. Vibronic Relaxation of Raman Modes in $CaMoO_4$ and $PbMoO_4$ Molecular Ionic Crystals. *Phys. Status Solidi C* **2004**, *1*, 3101−3105.
(26) Kovács, L.; Péter, Á.; Ivleva, L. I.; Baraldi, A.; Capelletti, R. Hydroxil Ions in Scheelite Type Molybdates and Tungstates. *Phys. Status Solidi C* **2007**, *4*, 856−859.
(27) Jian-Yu, C.; Qi-Ren, Z.; Ting-Yu, L.; Ze-Xu, S. Electronic Structures of $PbMoO_4$ Crystals with F-Type Colour Centres. *Chin. Phys. Lett.* **2007**, *24*, 1660−1663.
(28) Yevseyev, V. Radiation Effects on Optical Characteristic of $PbWO_4$. *Int. J. Mod. Phys. B* **2008**, *22*, 3695−3707.
(29) Fujita, M.; Itoh, M.; Mitani, H.; Sangeeta; Tyagi, M. Exciton Transition and Electronic Structure of $PbMoO_4$ Crystals Studied by Polarized Light. *Phys. Status Solidi B.* **2010**, *247*, 405−410.
(30) Yang, J. H.; Lu, C. H.; Su, H.; Ma, J. M.; Cheng, H. M.; Qi, L. M. Morphological and Structural Modulation of $PbWO_4$ Crystals Directed by Dextrans. *Nanotechnology* **2008**, *19*, 035608−035615.
(31) Longo, V. M.; et al. A Joint Experimental and Theoretical Study on the Nanomorphology of $CaWO_4$ Crystals. *J. Phys. Chem. C* **2011**, *115*, 20113−20119.
(32) Gracia, L.; Longo, V. M.; Cavalcante, L. S.; Beltran, A.; Avansi, W.; Li, M. S.; Mastelaro, V. R.; Varela, J. A.; Longo, E.; Andres, J. Presence of Excited Electronic State in $CaWO_4$ Crystals Provoked by a Tetrahedral Distortion: An Experimental and Theoretical Investigation. *J. Appl. Phys.* **2011**, *110*, 043501−043512.
(33) Bomio, M. R. D.; Cavalcante, L. S.; Almeida, M. A. P.; Tranquilin, R. L.; Batista, N. C.; Pizani, P. S.; Siu Li, M.; Andres, J.; Longo, E. Structural Refinement, Growth Mechanism, Infrared/Raman Spectroscopies and Photoluminescence Properties of $PbMoO_4$ Crystals. *Polyhedron* **2013**, *50*, 532−545.
(34) Sczancoski, J. C.; Bomio, M. R. D.; Cavalcante, L. S.; Joya, M. R.; Pizani, P. S.; Varela, J. A.; Longo, E.; Sui Li, M.; Andrés, J. A. Morphology and Blue Photoluminescence Emission of $PbMoO_4$ Processed in Conventional Hydrothermal. *J. Phys. Chem. C* **2009**, *113*, 5812−5822.
(35) Biswas, A.; Bayer, I. S.; Biris, A. S.; Wang, T.; Dervishi, E.; Faupel, F. Advances in Top-Down and Bottom-Up Surface Nanofabrication: Techniques, Applications & Future Prospects. *Adv. Colloid Interface Sci.* **2012**, *170*, 2−27.
(36) Biao, L.; Shu-Hong, Y.; Linjie, L.; Qiao, Z.; Fen, Z.; Ke, J. Morphology Control of Stolzite Microcrystals with High Hierarchy in Solution. *Angew. Chem., Int. Ed.* **2004**, *43*, 4745−4750.
(37) Shimodaira, Y.; Kato, H.; Kobayashi, H.; Kudo, A. Investigations of Electronic Structures and Photocatalytic Activities under Visible Light Irradiation of Lead Molybdate Replaced with Chromium[VI]. *Bull. Chem. Soc. Jpn.* **2007**, *80*, 885−893.
(38) Cui, X.; Yu, S. H.; Li, L.; Biao, L.; Li, H.; Mo, M.; Liu, X.-M. Selective Synthesis and Characterization of Single-Crystal Silver Molybdate/Tungstate Nanowires by a Hydrothermal Process. *Chem.—Eur. J.* **2004**, *10*, 218−223.
(39) Readman, J. E.; Lister, S. E.; Peters, L.; Wright, J.; Evans, J. S. O. Direct Synthesis of Cubic $ZrMo_2O_8$ Followed by Ultrafast in Situ Powder Diffraction. *J. Am. Chem. Soc.* **2009**, *131*, 17560−17562.
(40) Ito, T.; Takagi, H.; Asano, T. Drastic and Sharp Change in Color, Shape, and Magnetism in Transition of $CuMoO_4$ Single Crystals. *Chem. Mater.* **2009**, *21*, 3376−3379.
(41) Zeng, H. C. Synthesis of Stoichiometric Lead Molybdate $PbMoO_4$: An X-Ray Diffraction, Fourier Transform Infrared Spectroscopy, and Differential Thermal Analysis Study. *J. Mater. Res.* **1996**, *11*, 703−715.
(42) Arkady, Y.; Neiman, A. F. G.; Sharafutdinov, A. R. Origin of Potential Difference Self Generated by Reaction and Transport Processes. *Solid State Ionics* **1997**, *367*, 101−103.
(43) Zeng, H. C. Rectangular Vacancy Island Formation and Self-Depletion in Czochralski-grown $PbMoO_4$ Single Crystal During Heat Treatment. *J. Cryst. Growth.* **1996**, *160*, 119−128.
(44) Nakamura, T.; Sugiyama, K.; Moriguchi, E.; Shoji, T. Synthesis of Scheelite Group Minerals in the $CaWO_4$ - $CaMoO_4$ - $PbMoO_4$ - $PbWO_4$ System from Aqueous Solutions at 100 °C. *J. Min. Mater. Process. Inst. Jpn.* **2002**, *118*, 217−221.
(45) Pandey, P. K.; Bhave, N. S.; Kharat, R. B. Strutuctural, Optical, Electrical and Photovoltaic Electrochemical Studies of Cobalt Molybdates Thim Films. *Indian J. Pure Appl. Phys.* **2006**, *44*, 52−58.
(46) Ryu, J. H.; Koo, S. M.; Yoon, J. W.; Lim, C. S.; Shim, K. B. Synthesis of Nanocrystalline $MMoO_4$ (M = Ni, Zn) Phosphors Via a Citrate Complex Route Assisted by Microwave Irradiation and Their Photoluminescence. *Mater. Lett.* **2006**, *60*, 1702−1705.
(47) Phuruangrat, A.; Thongtem, T.; Thongtem, S. Analysis of Lead Molybdate and Lead Tungstate Synthesized by a Sonochemical Method. *Curr. Appl. Phys.* **2010**, *10*, 342−345.
(48) Kianpour, G.; Salavati-Niasari, M.; Emadi, H. Sonochemical Synthesis and Characterization of $NiMoO_4$ Nanorods. *Ultrason. Sonochem.* **2013**, *20*, 418−424.
(49) Di Chen, G. S.; Kaibin, T.; Zhenhua, L.; Huagui, Z. AOT-Microemulsions-Based Formation and Evolution of $PbWO_4$ Crystals. *J. Phys. Chem. B* **2004**, *108*, 11280−11284.

(50) Phuruangrat, A. T.; Thongtem, T.; Somchai, T. Synthesis of Lead Molybdate and Lead Tungstate via Microwave Irradiation Method. *J. Cryst. Growth* **2009**, *311*, 4076−4081.
(51) Thongtem, T.; Kungwankunakorn, S.; Kuntalue, B.; Phuruangrat, A.; Thongtem, S. Luminescence and Absorbance of Highly Crystalline $CaMoO_4$, $SrMoO_4$, $CaWO_4$ and $SrWO_4$ Nanoparticles Synthesized by Co-Precipitation Method at Room Temperature. *J. Alloys Compd.* **2010**, *506*, 475−481.
(52) Kianpour, G.; Salavati-Niasari, M.; Emadi, H. Precipitation Synthesis and Characterization of Cobalt Molybdates Nanostructures. *Superlattices Microstruct.* **2013**, *58*, 120−129.
(53) Cheng, Y.; Wang, Y.; Chen, D.; Bao, F. Evolution of Single Crystalline Dendrites from Nanoparticles Through Oriented Attachment. *J. Phys. Chem. B* **2005**, *109*, 794−798.
(54) Shen, M.; Zhang, Q.; Chen, H.; Peng, T. Hydrothermal Fabrication of $PbMoO_4$ Microcrystals with Exposed (001) Facets and its Enhanced Photocatalytic Properties. *Cryst. Eng. Comm.* **2011**, *13*, 2785−2791.
(55) Hashim, M.; Hu, C.; Wang, X.; Li, X.; Guo, D. Synthesis and Photocatalytic Property of Lead Molybdate Dendrites with Exposed (001) facet. *Appl. Surf. Sci.* **2012**, *258*, 5858−5862.
(56) Xing, G. J.; Liu, R.; Zhao, C.; Li, Y. L.; Wang, Y.; Wu, G. M. Photoluminescence and Photocatalytic Properties of Uniform $PbMoO_4$ Polyhedral Crystals Synthesized by Microemulsion-Based Solvothermal Method. *Ceram. Int.* **2011**, *37*, 2951−2956.
(57) Hernández-Uresti, D. B.; Martínez-de la Cruz, A.; Torres-Martínez, L. Photocatalytic Properties of $PbMoO_4$ Synthesized by Co-Precipitation Method: Organic Dyes Degradation under UV Irradiation. *Res. Chem. Intermed.* **2012**, *38*, 817−828.
(58) Martínez-de la Cruz, A.; Hernández-Uresti, D. B.; Torres-Martínez, L.; Lee, S. W. Photocatalytic Properties of $PbMoO_4$ Synthesized by a Hydrothermal Reaction. *React. Kinet., Mech. Catal.* **2012**, *107*, 467−475.
(59) Dickinson, R. G. The Crystal Structure of Wulfenite and Scheelite. *J. Am. Chem. Soc.* **1920**, *42*, 85−93.
(60) Gibbs, J. W.; Smith, A. W. On the Equilibrium of Heterogeneous Substances. *Trans. Conn. Acad. Arts Sci.* **1874**, *3*, 343−324.
(61) Wulff, G. *Zur F*rage der Geschwindigkeit Des Wachstums und Der Auflosung der Krystallflachen. *Z. Kristallogr. Miner.* **1901**, *34*, 1−8.
(62) Von Laue, M. Der Wulffsche Satz für Die Gleichgewichtsform von Kristallen. Kristallogr. die Gleichgewichtsform von Kristallen. *Z. Kristallogr.* **1943**, *105*, 124−133.
(63) Herring, C. Some Theorems on the Free Energies of Crystal Surfaces. *Phys. Rev.* **1951**, *82*, 87−93.
(64) Sun, C. Q. Size Dependence of Nanostructures: Impact of Bond Order Deficiency. *Solid State Chem.* **2007**, *35*, 1−159.
(65) Sun, C. Q. Dominance of Broken Bonds and Nonbonding Electrons at the Nanoscale. *Nanoscale* **2010**, *2*, 1930−1961.
(66) Liu, X. J.; Li, J. W.; Zhou, Z. F.; Yang, L. W.; Ma, Z. S.; Xie, G. F.; Pan, Y.; Sun, C. Q. Size-Induced Elastic Stiffening of ZnO Nanostructures: Skin-Depth Energy Pinning. *Appl. Phys. Lett.* **2009**, *94*, 131902−131905.
(67) Marks, L. D. Modified Wulff Constructions for Twinned Particles. *J. Cryst. Growth* **1983**, *61*, 556−566.
(68) Gracia, L.; Beltrán, A.; Andrés, J. Characterization of the High-Pressure Structures and Phase Transformations in $SnO_2$. A Density Functional Theory Study. *J. Phys. Chem. B* **2007**, *111*, 6479−6485.
(69) Stroppa, D. G.; et al. Unveiling the Chemical and Morphological Features of Sb−$SnO_2$ Nanocrystals by the Combined Use of High-Resolution Transmission Electron Microscopy and ab Initio Surface Energy Calculations. *J. Am. Chem. Soc.* **2009**, *131*, 14544−14548.
(70) Gracia, L.; Andrés, J.; Longo, V. M.; Varela, J. A.; Longo, E. A Theoretical Study on the Photoluminescence of $SrTiO_3$. *Chem. Phys. Lett.* **2010**, *493*, 141−146.
(71) Itoh, M.; Kajitani, T. Polarized Luminescence from Jahn-Teller Split Triplet States of Self-Trapped Excitons in $PbMoO_4$. *Phys. Rev. B* **2013**, *87*, 085201−085208.
(72) Wong-Ng, W.; McMurdie, H. F.; Hubbard, C. R.; Mighell, A. D. JCPDS-ICDD Research Associateship (Cooperative Program with NBS/NIST). *J. Res. Natl. Inst. Stand. Technol.* **2001**, *106*, 1013−1028.
(73) Lutterotti, L. Total Pattern Fitting for the Combined Size−Strain−Stress−Texture Determination in Thin Film Diffraction. *Nucl. Instrum. Methods, B* **2010**, *268*, 334−340.
(74) Lutterotti, L.; Bortolotti, M.; Ischia, G.; Lonardelli, I.; Wenk, H. R. Rietveld Texture Analysis from Diffraction Images. *Z. Kristallogr. Suppl.* **2007**, *2007*, 125−130.
(75) Rousseau, D. L.; Baumann, R. P.; Porto, S. P. S. Normal Mode Determination in Crystals. *J. Raman Spectrosc.* **1981**, *10*, 253−290.
(76) Porto, S. P. S.; Scott, J. F. Raman Spectra of $CaWO_4$, $SrWO_4$, $CaMoO_4$, and $SrMoO_4$. *Phys. Rev.* **1967**, *157*, 716−719.
(77) Ling, Z. C.; Xia, H. R.; Ran, D. G.; Liu, F. Q.; Sun, S. Q.; Fan, J. D.; Zhang, H. J.; Wang, J. Y.; Yu, L. L. Lattice Vibration Spectra and Thermal Properties of $SrWO_4$ Single Crystal. *Chem. Phys. Lett.* **2006**, *426*, 85−90.
(78) Basiev, T. T.; Sobol, A. A.; Voronko, Y. K.; Zverev, P. G. Spontaneous Raman Spectroscopy of Tungstate and Molybdate Crystals for Raman Lasers. *Opt. Mater.* **2000**, *15*, 205−216.
(79) Yu, C. L.; et al. Structural and Electrical Properties of $PbMoO_4$ Under High Pressure. *J. Phys.: Condens. Matter* **2007**, *19*, 425215−425222.
(80) Jayaraman, A.; Batlogg, B.; Van Uitert, L. G. Effect of High Pressure on the Raman and Electronic Absorption Spectra of $PbMoO_4$ and $PbWoO_4$. *Phys. Rev. B* **1985**, *31*, 5423−5427.
(81) Moraes, E.; Bomio, M. R. D.; Longo, V. M.; Longo, E.; Varela, J. A. Freezing Distortions and Photoluminescence Property in $PbMoO_4$ Micro-Octahedrons: An Experimental and Theoretical Study. *Curr. Phys. Chem.* **2013**, *3*, In Press.
(82) Basiev, T. T.; Vassiliev, S. V.; Konjushkin, V. A.; Osiko, V. V.; Zagumennyi, A. I.; Zavartsev, Y. D.; Kutovoi, S. A.; Shcherbakov, I. A. Diode Pumped 500-ps Nd:$GdVO_4$ Raman Laser. *Laser Phys. Lett.* **2004**, *1*, 237−240.
(83) Voron'ko, Y. K.; Sobol', A. A.; Shukshin, V. E.; Zagumennyĭ, A. I.; Zavartsev, Y. D.; Kutovoĭ, S. A. Raman Spectroscopic Study of Structural Disordering in $YVO_4$, $GdVO_4$, and $CaWO_4$ Crystals. *Phys. Solid State* **2009**, *51*, 1886−1893.
(84) See http://www.jcrystal.com/ (accessed Jan 26, 2013).
(85) See http://www.jcrystal.com/jcrystal (accessed Jan 26, 2013).
(86) Yang, W. D.; Haile, S. M. Influences of Water Content on Synthesis of $(Pb_{0.5},Ba_{0.5})TiO_3$ Materials Using Acetylacetone as Chelating Agent in a Sol−Gel Process. *J. Eur. Ceram. Soc.* **2006**, *26*, 3203−3210.
(87) Raykar, V. S.; Singh, A. K. Thermal and Rheological Behavior of Acetylacetone Stabilized ZnO Nanofluids. *Therm. Acta.* **2010**, *502*, 60−65.
(88) Uchiyama, H.; Takagi, K.; Kozuka, H. Solvothermal Synthesis of Size-Controlled $ZrO_2$ Microspheres via Hydrolysis of Alkoxides Modified with Acetylacetone. *Colloids Surf. A: Physicochem. Eng. Aspects* **2012**, *403*, 121−128.
(89) Weng, L.; Bao, X.; Sagoe-Crentsil, K. Effect of Acetylacetone on the Preparation of PZT Materials in Sol−Gel Processing. *Mater. Sci. Eng., B* **2002**, *96*, 307−312.
(90) Penn, R. L.; Banfield, J. F. Morphology Development and Crystal Growth in Nanocrystalline Aggregates under Hydrothermal Conditions: Insights from Titania. *Geochim. Cosmochim. Acta* **1999**, *63*, 1549−1557.
(91) Penn, R. L.; Banfield, J. F. Imperfect Oriented Attachment: Dislocation Generation in Defect-Free Nanocrystals. *Science* **1998**, *281*, 969−971.
(92) Wu, X.; Du, J.; Li, H.; Zhang, M.; Xi, B.; Fan, H.; Zhu, Y.; Qian, Y. Aqueous Mineralization Process to Synthesize Uniform Shuttle-Like $BaMoO_4$ Microcrystals at Room Temperature. *J. Solid State Chem.* **2007**, *180*, 3288−3295.
(93) Ryu, E. K.; Huh, Y. D. Synthesis of Hierarchical Self-Assembled $BaMoO_4$ Microcrystals. *Bull. Korean Chem. Soc.* **2008**, *29*, 503−506.

(94) Scopece, D. SOWOS: An Open-Source Program for the Three-Dimensional Wulff Construction. *J. Appl. Crystallogr.* **2013**, *46*, 811−816.
(95) Chu, H.; Li, X.; Chen, G.; Jin, Z.; Zhang, Y.; Li, Y. Inorganic Hierarchical Nanostructures Induced by Concentration Difference and Gradient. *Nano Res.* **2008**, *1*, 213−220.
(96) Wood, D. L.; Tauc, J. Weak Absorption Tails in Amorphous Semiconductors. *Phys. Rev. B* **1972**, *5*, 3144−3151.
(97) Lacomba-Perales, R.; Ruiz-Fuertes, J.; Errandonea, D.; Martinez-Garcia, D.; Segura, A. Optical Absorption of Divalent Metal Tungstate: Correlation Between the Band-Gap Energy and the Cation Ionic Radius. *Europhys. Lett.* **2008**, *83*, 37002−37007.
(98) Longo, V. M.; Cavalcante, L. S.; Paris, E. C.; Sczancoski, J. C.; Pizani, P. S.; Li, M. S.; Andrés, J.; Longo, E.; Varela, J. A. Hierarchical Assembly of $CaMoO_4$ Nano-Octahedrons and Their Photoluminescence Properties. *J. Phys. Chem. C* **2011**, *115*, 5207−5919.
(99) Hernández-Uresti, D.; Martínez-de la Cruz, A.; Torres-Martínez, L. Photocatalytic Properties of $PbMoO_4$ Synthesized by Co-Precipitation method: Organic Dyes Degradation under UV Irradiation. *Res. Chem. Intermed.* **2012**, *38*, 817−828.
(100) Chen, Q.; Wu, Q. Fabrication of Carbon Microspheres@ $PbMoO_4$ Core−Shell Hybrid Structures and Its Visible Light-Induced Photocatalytic Activity. *Catal. Commun.* **2012**, *24*, 85−89.
(101) Dai, K.; Yao, Y.; Liu, H.; Mohamed, I.; Chen, H.; Huang, Q. Enhancing the Photocatalytic Activity of Lead Molybdate by Modifying with Fullerene. *J. Mol. Catal. A: Chem.* **2013**, *375*, 111−117.
(102) Cavalcante, L. S.; Sczancoski, J. C.; Batista, N. C.; Longo, E.; Varela, J. A.; Orlandi, M. O. Growth Mechanism and Photocatalytic Properties of $SrWO_4$ Microcrystals Synthesized by Injection of Ions into a Hot Aqueous Solution. *Adv. Powder Technol.* **2013**, *24*, 344−353.
(103) Zhang, Y.; Holzwarth, N. A. W.; Williams, R. T. Electronic Band Structures of the Scheelite Materials $CaMoO_4$, $CaWO_4$, $PbMoO_4$, and $PbWO_4$. *Phys. Rev. B* **1998**, *57*, 12738−12750.